https://doi.org/10.5194/hess-2019-622
Preprint. Discussion started: 3 January 2020
© Author(s) 2020. CC BY 4.0 License.

Hydrology and Earth System Sciences
Discussions
Open Access
EGU

A reduced-order model for dual state-parameter geostatistical inversion

Yu-Li Wang[1], Tian-Chyi Jim Yeh[1], Jui-Pin Tsai[2,*]

1. Department of Hydrology and Atmospheric Sciences, University of Arizona, Arizona, United States.

2. Department of Bioenvironmental Systems Engineering, National Taiwan University, Taiwan.

* Corresponding Author

Assistant Professor Jui-Pin Tsai, jptsai@ntu.edu.tw

https://doi.org/10.5194/hess-2019-622
Preprint. Discussion started: 3 January 2020
© Author(s) 2020. CC BY 4.0 License.
Hydrology and Earth System Sciences Discussions
Open Access

0. Abstract

To properly account the subsurface heterogeneity, geostatistical inverse models usually permit enormous amount of spatial correlated parameters to interpret the collected states. Several reduced-order techniques for the brick domain are investigated to leverage the memory burden of parameter covariance. Their capability to irregular domain is limited. Furthermore, due to the over fitting of states, the estimated parameters usually diverge to unreasonable values. Although some propriate tolerances can be used to eliminate this problem, they are presumed and heavily rely on the personal judgement. To address these two issues, we present a model reduction technique to the irregular domain by singular value decomposition (SVD). Afterward, the state errors and parameters are sequentially updated to leverage the over fitting. The computational advantages of the proposed reduced-order dual state-parameter inverse algorithm are demonstrated through two numerical experiments and one case study in a catchment scale field site. The investigations suggest that the stability of convergence dramatically improves. The estimated parameter values stabilize to reasonable order of magnitude. In addition, the memory requirement significantly reduces while the resolution of estimate preserves. The proposed method benefits multi-discipline scientific problems, especially useful and convenient for assimilating different types of measurements.

https://doi.org/10.5194/hess-2019-622
Preprint. Discussion started: 3 January 2020
© Author(s) 2020. CC BY 4.0 License.

1. Introduction

Groundwater is one of the necessary resources in many regions where the amount of rainfall and the capacity of reservoir is limited. To provide enough fresh water for the current and future uses in these areas, proper water resources management and contaminated site remediation strategies are required, which relies on the understanding of the site-specific spatial distribution of hydrological parameters (e.g., hydraulic conductivity and specific storage) in the prefer scale.

Many covariance based geostatistical approaches have been widely employed for aquifer characterization. Several previous studies suggested that the geostatistical inversion is superior than many other subsurface inverse modeling because it estimates the uncertainty and has ability to assimilate different type of observed data sequentially (Vesselinov et al., 2001). However, as pointed out by Illman et al. (2015), when the number of observations and unknown parameters are huge, the primary drawbacks of geostatistical inversion are the computational and memory burdens.

Several ensemble approaches have been proposed to handle the memory and large covariance matrices. For instance, Particle Filter or Sequential Monte Carlo method (SMC, Field et al., 2016; Zhang et al., 2017), iterative Ensemble Kalman Filter (EnKF, Schöniger et al., 2012; Ait-El-Fquih et al., 2016), iterative Ensemble Smoother (ES, Zhang et al., 2018), Extended Kalman Filter (EKF, Yeh and Huang 2005; Leng and Yeh, 2003), and many other related methods construct the covariance between the parameter and state variable from a set of ensemble member. Since a bunch of realizations (usually several hundreds or thousands) are required to infer the population covariance from the sample covariance, the algorithm may not be computational affordable when the simulation time of single forward modeling is time consuming.

On the other hand, Quasi-Linear Geostatistical Approach (QLGA, Kitanidis,

https://doi.org/10.5194/hess-2019-622
Preprint. Discussion started: 3 January 2020
© Author(s) 2020. CC BY 4.0 License.

1995) and Successive Linear Estimator (SLE, Yeh et al., 1996) avoid generating a large set of ensemble realizations. They construct the parameter covariance by some prior knowledge of unknown parameter field (e.g., covariance function, variance, and correlation length). Afterward, the covariance between the parameter and state variable is estimated through the sensitivity of state variable with respect to parameter. This approach requires significant amount of memory resource when the number of unknown parameter and state variable are huge. Furthermore, evaluating the sensitivity efficiently may be a difficult task for some scientific problems. As a result, considerable efforts are devoted to improving the capability of the algorithm. For instance, Sun and Yeh (1990) employed the adjoint approach to evaluate the sensitivity. It reduces the cost of running forward model from the order of number of unknown parameters to the number of state measurements. Saibaba and Kitanidis (2012) incorporates the hierarchical matrices technique with a matrix-free Krylov subspace approach to improve the computational efficiency. Liu et al. (2014) avoids the direct solution of sensitivity matrix by the Krylov subspace method. Li et al. (2015) and Zha et al. (2018) project the covariance matrix on the orthonormal basis and evaluate the cross product of sensitivity and squared root covariance directly using finite differencing approach. This method eliminates the sensitivity evaluation and reduces the computational cost of running forward model to the order of number of leading modes. Li et al. (2014) take the advantage of hierarchical nature of matrices to accelerate the computation of dense matrix vector products and rewrite the Kalman filtering equations into a computational efficient manner. Ghorbanidehno et al. (2015) extend their approach to the general case of non-linear dynamic systems. Similarly, Lin et al. (2016) reduces the computational complexity by projecting the parameters to different hierarchies of Krylov subspace. Pagh (2013) use fast Fourier transform to speed up the computation of covariance matrix multiplication. In addition, many

https://doi.org/10.5194/hess-2019-622
Preprint. Discussion started: 3 January 2020
© Author(s) 2020. CC BY 4.0 License.
Hydrology and Earth System Sciences
Open Access
Discussions

approaches reduce the computational cost and memory requirement. For example, Nowak and Litvinenko (2013) combine low rank approximations to the covariance matrices with fast Fourier transform; Kitanidis (2015) decomposes the covariance matrix by some orthonormal basis and shows that the choice of basis can be tailored to the problem of interest to improve estimation accuracy; Li et al. (2015) use discrete cosine transform to compress the data covariance matrix of a 1-D state variable series; Zha et al. (2018) use Karhunen-Loeve Expansion to compress the parameter covariance matrix of a 3-D parameter field. Other useful reduced order models are Galerkin projection (Liu et al., 2013), principal component (Kitanidis and Lee, 2014), randomized algorithm (Lin et al., 2017), Whittaker-Shannon interpolation (Horning et al., 2019), and Kronecker product decomposition (Zunino and Mosegaard, 2019).

In addition to reformulate the covariance matrix, the temporal moments eliminate the temporal derivative term in the governing equation. Thus, it is another potential method to reduce the data size and computational cost (Cirpka and Kitanidis, 2000; Nowak and Cirpka, 2006; Yin and Illman, 2009).

There are several limitations exist in the previous geostatistical inverse algorithms. The first issue is over calibration or over fitting. During the inverse process, the calibration terminates when the difference between the observed and simulated states reduces to the value smaller than the given tolerance, an arbitrary value based on user's personal judgement. In practical, the tolerance is determined by the expected numeric and measurement errors. Since its true order of magnitude is unknow, the estimated parameter field sometimes diverges if the tolerance is underestimated. To be specific, the estimated parameters will first converge to the best values accompanied with the successive assimilation of the information about the subsurface heterogeneity embedded in the observed state variables. The values of parameter then diverge to the unreasonable huge or small values to compensate the

© Author(s) 2020. CC BY 4.0 License.

numeric and measurement errors. This instability is not user friendly because the reasonable (i.e., converged) estimate needs to be selected manually. Furthermore, when different types of measurement (e.g., water level, flux, temperature, gravity, etc.) are available, it is suggested that assimilate these data sequentially is a more robust approach than the simultaneous assimilation (Tsai et al., 2017). Accordingly, the manually determination of convergence prohibits the automatic sequential assimilation.

Second, when dealing with a 2-D or 3-D parameter or state variable fields, a specific matrix structures are required to efficiently decompose the unconditional covariance matrix to the orthonormal basis. For instance, a regular grid spacing is required to efficiently perform the fast Fourier transform (Nowak and Litvinenko, 2013) and discrete cosine transform (Li et al., 2015). Similarly, Karhunen-Loeve Expansion (Zha et al., 2018) requires a brick or rectangle shape domain and grid. This requirement comes from the derivation of analytic eigenvalue and eigenvector of a separable exponential function.

To overcome these two existing limitations, we first introduce an additional step to estimate the error of state variables based on the error covariance matrices. Next, we derive a reduced order model using singular value decomposition. Afterward, we present a matrix manipulation method to eliminate the requirement of brick or rectangle domain during constructing the eigenvalue and eigenvector of unconditional covariance matrix.

This paper is arranged as follows. We first revisit the SLE that forms the geostatistical inversion approach (section 2.2). Thereafter, the algorithm is reformulated by collaborating with the data error, reduced order approach (i.e. singular value decomposition, SVD), and irregular domain (section 2.3). Furthermore, a perturbation method is proposed to improve the efficiency of covariance evaluation

https://doi.org/10.5194/hess-2019-622
Preprint. Discussion started: 3 January 2020
© Author(s) 2020. CC BY 4.0 License.

process (section 2.4). In section 3, we test the proposed dual state-parameter estimation algorithm with two synthetic examples and a tomographic survey at the field site to demonstrate the superiority of the proposed method. Lastly, summary and conclusions are presented.

2.1. Groundwater Flow Model.

The 2-D groundwater flow in heterogeneous confined aquifer can be described as

$$\nabla \cdot [T(\mathbf{x}) \cdot \nabla h(\mathbf{x},t)] = S(\mathbf{x}) \frac{\partial h(\mathbf{x},t)}{\partial t} \quad (1)$$

where h is the head responses (m), T is hydraulic transmissivity (m^2/day), S is storage coefficient (-), $\mathbf{x}$ is the vector in x and y directions, and t represents time (day).

2.2. Reduced order successive linear estimator

The singular value decomposition (SVD) is employed to reduce the order of the parameter covariance, leading to less memory requirement and more computational efficiency inverse exercise. Afterward, the data error is considered to improve the stability of convergence.

(1) Hard Data

When the hard data are available, kringing is used to estimate the conditional parameter field and the corresponding conditional covariance matrix from the measured parameters. It is expressed as

$$\hat{\mathbf{f}}^{(1)} = \hat{\mathbf{f}}^{(0)} + \boldsymbol{\varepsilon}_{ff}^{(0)} \mathbf{C} \mathbf{R}_{f^*f^*}^{-1} [\mathbf{f}^* - \hat{\mathbf{f}}^{(0)}] \quad (3)$$

and

$$\boldsymbol{\varepsilon}_{ff}^{(1)} = \boldsymbol{\varepsilon}_{ff}^{(0)} - \boldsymbol{\varepsilon}_{ff}^{(0)} \mathbf{C} \mathbf{R}_{f^*f^*}^{-1} \mathbf{C}^T \boldsymbol{\varepsilon}_{ff}^{(0)} \quad (4)$$

in which $\mathbf{f}^*$ (n_m×1) is the measured parameters, $\hat{\mathbf{f}}^{(0)}$ (n_f×1) is the unconditional parameter field, $\hat{\mathbf{f}}^{(1)}$ (n_f×1) is the conditional parameter field. n_f represents the number of unknown parameters and n_m represents the number of measured parameters. $\boldsymbol{\varepsilon}_{ff}^{(0)}\mathbf{C}$ and $\mathbf{C}^T\boldsymbol{\varepsilon}_{ff}^{(0)}$ (n_m×n_f) are the unconditional parameter covariance matrices depicting the spatial correlation between the measured parameters and all parameters. $\boldsymbol{\varepsilon}_{ff}^{(0)}$ (n_f×n_f) is the unconditional parameter covariance matrix depicting the spatial correlation between all parameters ($\hat{\mathbf{f}}$). $\mathbf{C}$ (n_f×n_m) is a matrix eliminating the column in $\boldsymbol{\varepsilon}_{ff}^{(0)}$ when the corresponding measured parameter is absent. $\boldsymbol{\varepsilon}_{ff}^{(1)}$ (n_f×n_f) is the conditional covariance marix of all parameters. The diagonal term of the matrix (i.e., residual variance) represents the remaining uncertainty of the estimated parameter after the information (measurements) is included. A small residual variance indicates the spatial trend of estimated parameter is close to the true, while a large value indicates the estimate is close to the initial guessed value (i.e. heterogeneity is not resolved). $\mathbf{R}_{f^*f^*}$ (n_m×n_m) is the covariance matrix depicting the correlation between measured parameters. Notice that Cholesky and QR decompositions are utilized to solve the matrix multiplication of inverse $\mathbf{R}_{f^*f^*}$ when it is and is not a positive definite matrix.

Since n_f is usually huge, storage demand of $\boldsymbol{\varepsilon}_{ff}^{(0)}$ and $\boldsymbol{\varepsilon}_{ff}^{(1)}$ may not be always affordable. Thus, singular value decomposition (SVD) is utilized to relieve this memory burden by keeping the leading eigenvalues and eigenvectors. The SVD of $\boldsymbol{\varepsilon}_{ff}$ is expressed as

$$\boldsymbol{\varepsilon}_{ff} = \mathbf{g}\,\boldsymbol{\lambda}\,\mathbf{g}^T \quad (5)$$

where $\boldsymbol{\lambda}$ (n_{svd}×n_{svd}) is eigenvalues, $\mathbf{g}$ (n_f×n_{svd}) is eigenvectors, and n_{svd} is number

https://doi.org/10.5194/hess-2019-622
Preprint. Discussion started: 3 January 2020
© Author(s) 2020. CC BY 4.0 License.

of leading eigenvalues. Substitute eq. (5) into eqs. (3) and (4), we have

$$\hat{\mathbf{f}}^{(1)} = \hat{\mathbf{f}}^{(0)} + \mathbf{g}^{(0)}\boldsymbol{\lambda}^{(0)}\mathbf{g}^{(0)T}\mathbf{CR}_{ff}^{-1}[\mathbf{f}^{*} - \hat{\mathbf{f}}^{(0)}] \quad (6)$$

and

$$\mathbf{g}^{(1)}\boldsymbol{\lambda}^{(1)}\mathbf{g}^{(1)T} = \mathbf{g}^{(0)}\boldsymbol{\lambda}^{(0)}\mathbf{g}^{(0)T} - \mathbf{g}^{(0)}\boldsymbol{\lambda}^{(0)}\mathbf{g}^{(0)T}\mathbf{CR}_{ff}^{-1}\mathbf{C}^{T}\mathbf{g}^{(0)}\boldsymbol{\lambda}^{(0)}\mathbf{g}^{(0)T} \quad (7)$$

Since $\mathbf{g}^{(1)}$ is always a function of $\mathbf{g}^{(0)}$, it can be expressed as

$$\mathbf{g}^{(1)} = \mathbf{g}^{(0)}\mathbf{u}^{(0)} \quad (8)$$

where is $\mathbf{u}^{(0)}$ ($n_{svd}\times n_{svd}$) is the matrix transferring the information of spatial correlation of parameters to the next iteration. Accordingly, eq. (7) can reduce to

$$\mathbf{u}^{(0)}\boldsymbol{\lambda}^{(1)}\mathbf{u}^{(0)T} = \sqrt{\boldsymbol{\lambda}^{(0)}}(\mathbf{I} - \sqrt{\boldsymbol{\lambda}^{(0)}}\mathbf{g}^{(0)T}\mathbf{CR}_{f^{*}f^{*}}^{-1}\mathbf{C}^{T}\mathbf{g}^{(0)}\sqrt{\boldsymbol{\lambda}^{(0)}})\sqrt{\boldsymbol{\lambda}^{(0)}} \quad (9)$$

in which $\mathbf{I}$ is an identity matrix. By decomposing eq. (9) with SVD, we obtain the updated eigenvalue $\boldsymbol{\lambda}^{(1)}$ and $\mathbf{u}^{(0)}$. The updated eigenvector $\mathbf{g}^{(1)}$ can be evaluated by eq. (8).

(2) Error of Soft Data

After considering the hard data, the inherently presented data errors (e.g., measurement, numeric, round-off, truncation errors, etc.) are included prior to the parameter estimation. The estimated data error and the corresponding covariance matrix are expressed as

$$\hat{\mathbf{e}}^{(r+1)} = \hat{\mathbf{e}}^{(r)} + \boldsymbol{\varepsilon}_{hh}^{(r)}[\mathbf{J}_{fh}^{(r)T}\boldsymbol{\varepsilon}_{ff}^{(r)}\mathbf{J}_{fh}^{(r)} + \boldsymbol{\varepsilon}_{hh}^{(r)}]^{-1}[\mathbf{h}^{(r)} - (\mathbf{h}^{*} + \hat{\mathbf{e}}^{(r)})] \quad (10)$$

and

$$\boldsymbol{\varepsilon}_{hh}^{(r+1)} = \boldsymbol{\varepsilon}_{hh}^{(r)} - \boldsymbol{\varepsilon}_{hh}^{(r)}[\mathbf{J}_{fh}^{(r)T}\boldsymbol{\varepsilon}_{ff}^{(r)}\mathbf{J}_{fh}^{(r)} + \boldsymbol{\varepsilon}_{hh}^{(r)}]^{-1}\boldsymbol{\varepsilon}_{hh}^{(r)} \quad (11)$$

in which $\mathbf{h}^{*}$ ($n_d\times 1$) is the observed head and $\mathbf{h}^{(r)}$ ($n_d\times 1$) is the simulated head based on the estimated parameters from the r^{th} iteration. n_d represents the number of measured state variables. The superscript r is the iteration index starting from one.

$\boldsymbol{\varepsilon}_{hh}^{(1)}$ ($n_d \times n_d$) is the unconditional covariance matrix of the observed head. The diagonal terms represent the uncertainty of the measurement and the off diagonal terms represent the correlation between errors. $\boldsymbol{\varepsilon}_{hh}^{(r)}$ and $\boldsymbol{\varepsilon}_{hh}^{(r+1)}$ ($n_d \times n_d$) are the conditional covariance matrices. $\hat{\mathbf{e}}^{(1)}$ ($n_d \times 1$) is the initial data error. $\hat{\mathbf{e}}^{(r)}$ and $\hat{\mathbf{e}}^{(r+1)}$ ($n_d \times 1$) are the estimated data error. $\mathbf{J}_{fh}^{(r)}$ ($n_f \times n_d$) is the sensitivity of observed head with respect to the estimated parameters during the r^{th} iteration.

The weight (i.e., $\mathbf{W}^{(r)} = \boldsymbol{\varepsilon}_{hh}^{(r)} [\mathbf{J}_{fh}^{(r)T} \boldsymbol{\varepsilon}_{ff}^{(r)} \mathbf{J}_{fh}^{(r)} + \boldsymbol{\varepsilon}_{hh}^{(r)}]^{-1}$) is a combination of observed head covariance matrix ($\boldsymbol{\varepsilon}_{hh}^{(r)}$) and simulated head covariance matrix ($\mathbf{R}_{hh}^{(r)} = \mathbf{J}_{fh}^{(r)T} \boldsymbol{\varepsilon}_{ff}^{(r)} \mathbf{J}_{fh}^{(r)}$). It represents the ratio of data error ($\boldsymbol{\varepsilon}_{hh}^{(r)}$, including numeric and measurement errors) to the total error ($\mathbf{R}_{hh}^{(r)} + \boldsymbol{\varepsilon}_{hh}^{(r)}$, including model structure, parameter, numeric, and measurement errors). When the model is poorly calibrated, the simulated head based on the current model structure and parameter values is much uncertain than that of observed head (i.e. $\mathbf{R}_{hh}^{(r)} >> \boldsymbol{\varepsilon}_{hh}^{(r)}$). Thus, the weight ($\mathbf{W}^{(r)}$) is small and the algorithm trusts the observation ($\mathbf{h}^*$) more than the prediction ($\mathbf{h}^{(r)}$). After assimilating the subsurface characteristic casted in the observation, the uncertainty of simulated head ($\mathbf{R}_{hh}^{(r)}$) reduces and the algorithm trusts the observation ($\mathbf{h}^*$) less than the prediction ($\mathbf{h}^{(r)}$). Therefore, dismiss between $\mathbf{h}^*$ and $\mathbf{h}^{(r)}$ are reflected into $\hat{\mathbf{e}}^{(r)}$. This data error calibration step is similar to the Kalman filter, but instead of using the observation from previous time step only, we consider all of the available observation simultaneously.

Again, substitute eigenvalue $\boldsymbol{\lambda}$ and eigenvector $\mathbf{g}$ of $\boldsymbol{\varepsilon}_{ff}^{(r)}$ expressed in eq. (5), the reduced order formulations of eqs. (10) and (11) are

https://doi.org/10.5194/hess-2019-622
Preprint. Discussion started: 3 January 2020
© Author(s) 2020. CC BY 4.0 License.

$$\hat{\mathbf{e}}^{(r+1)} = \hat{\mathbf{e}}^{(r)} + \boldsymbol{\varepsilon}_{hh}^{(r)}[\mathbf{H}_{fh}^{(r)}\mathbf{H}_{fh}^{(r)T} + \boldsymbol{\varepsilon}_{hh}^{(r)}]^{-1}[\mathbf{h}^{(r)} - (\mathbf{h}^{*} + \hat{\mathbf{e}}^{(r)})] \quad (12)$$

and

$$\boldsymbol{\varepsilon}_{hh}^{(r+1)} = \boldsymbol{\varepsilon}_{hh}^{(r)} - \boldsymbol{\varepsilon}_{hh}^{(r)}[\mathbf{H}_{fh}^{(r)}\mathbf{H}_{fh}^{(r)T} + \boldsymbol{\varepsilon}_{hh}^{(r)}]^{-1}\boldsymbol{\varepsilon}_{hh}^{(r)} \quad (13)$$

where $\mathbf{H}_{fh}^{(r)}$ ($n_d \times n_{svd}$) is

$$\mathbf{H}_{fh}^{(r)} = \mathbf{J}_{fh}^{(r)T}\mathbf{g}^{(r)}\sqrt{\boldsymbol{\lambda}^{(r)}} \quad (14)$$

Notice that if the number of state (n_d) is huge, SVD can potentially be used to decompose $\boldsymbol{\varepsilon}_{hh}^{(r)}$ (eq. 5) and reduce the storage requirement.

(3) Soft Data.

After estimating the data error, the measured state variables and data errors are substituted into successive linear estimator (SLE) (Yeh et al., 1996) to estimate the conditional parameter fields and the corresponding residual covariance matrix:

$$\hat{\mathbf{f}}^{(r+1)} = \hat{\mathbf{f}}^{(r)} + \boldsymbol{\varepsilon}_{ff}^{(r)}\mathbf{J}_{fh}^{(r)}[\mathbf{J}_{fh}^{(r)T}\boldsymbol{\varepsilon}_{ff}^{(r)}\mathbf{J}_{fh}^{(r)} + \boldsymbol{\varepsilon}_{hh}^{(r+1)}]^{-1}[(\mathbf{h}^{*} + \hat{\mathbf{e}}^{(r+1)}) - \mathbf{h}^{(r)}] \quad (15)$$

and

$$\boldsymbol{\varepsilon}_{ff}^{(r+1)} = \boldsymbol{\varepsilon}_{ff}^{(r)} - \boldsymbol{\varepsilon}_{ff}^{(r)}\mathbf{J}_{fh}^{(r)}[\mathbf{J}_{fh}^{(r)T}\boldsymbol{\varepsilon}_{ff}^{(r)}\mathbf{J}_{fh}^{(r)} + \boldsymbol{\varepsilon}_{hh}^{(r+1)}]^{-1}\mathbf{J}_{fh}^{(r)T}\boldsymbol{\varepsilon}_{ff}^{(r)} \quad (16)$$

The reduced order version of SLE can be derived by substitute eq. (5) into eqs. (15) and (16). That is,

$$\hat{\mathbf{f}}^{(r+1)} = \hat{\mathbf{f}}^{(r)} + \mathbf{g}^{(r)}\sqrt{\boldsymbol{\lambda}^{(r)}}\mathbf{H}_{fh}^{(r)T}[\mathbf{H}_{fh}^{(r)}\mathbf{H}_{fh}^{(r)T} + \boldsymbol{\varepsilon}_{hh}^{(r+1)}]^{-1}[(\mathbf{h}^{*} + \hat{\mathbf{e}}^{(r+1)}) - \mathbf{h}^{(r)}] \quad (17)$$

and

$$\mathbf{g}^{(r+1)}\boldsymbol{\lambda}^{(r+1)}\mathbf{g}^{(r+1)T} = \mathbf{g}^{(r)}\boldsymbol{\lambda}^{(r)}\mathbf{g}^{(r)T} - \mathbf{g}^{(r)}\sqrt{\boldsymbol{\lambda}^{(r)}}\mathbf{H}_{fh}^{(r)T}[\mathbf{H}_{fh}^{(r)}\mathbf{H}_{fh}^{(r)T} + \boldsymbol{\varepsilon}_{hh}^{(r+1)}]^{-1}\mathbf{H}_{fh}^{(r)}\sqrt{\boldsymbol{\lambda}^{(r)}}\mathbf{g}^{(r)T} \quad (18)$$

Using eq. (8), eq. (18) further reduces to

$$\mathbf{u}^{(r)}\boldsymbol{\lambda}^{(r+1)}\mathbf{u}^{(r)T} = \sqrt{\boldsymbol{\lambda}^{(r)}}(\mathbf{I} - \mathbf{H}_{fh}^{(r)T}[\mathbf{H}_{fh}^{(r)}\mathbf{H}_{fh}^{(r)T} + \boldsymbol{\varepsilon}_{hh}^{(r+1)}]^{-1}\mathbf{H}_{fh}^{(r)})\sqrt{\boldsymbol{\lambda}^{(r)}} \quad (19)$$

By decomposing eq. (19) with SVD, we can evaluate the updated eigenvalue $\boldsymbol{\lambda}^{(r+1)}$

and $\mathbf{u}^{(r)}$. The updated eigenvector $\mathbf{g}^{(r+1)}$ then can be calculated by eq. (8).

(4) Convergence Criterion

The estimated field is considered as the converge one when the spatial variance of the estimated parameter duing several iterations are steady. The tolarence using mean squared error between the observed and simulated states is no longer necessary.

2.3. Required Inputs

To initiate the algorithm, the initial guess of parameter field $\hat{\mathbf{f}}^{(0)}$ and data error $\hat{\mathbf{e}}^{(0)}$, as well as the unconditional covariance matrix of the parameters $\boldsymbol{\varepsilon}_{ff}^{(0)}$ and observed data $\boldsymbol{\varepsilon}_{hh}^{(0)}$ are required. The details are explained as followings:

Parameter Field: The initial parameter field $\hat{\mathbf{f}}^{(0)}$ can be any reasonable values based on the prior knowledge.

Parameter Covariance: We assume the unconditional parameter covariance matrix is defined by an exponential covariance function

$$\boldsymbol{\varepsilon}_{ff}^{(0)} = Var \cdot \exp\left(\frac{-|\mathbf{d}_\mathbf{x}|}{\lambda_x} + \frac{-|\mathbf{d}_\mathbf{y}|}{\lambda_y} \right) \quad (20)$$

where Var represents the unconditional spatial variance of the parameter; $\mathbf{d}_\mathbf{x}$ (n_f×1) and $\mathbf{d}_\mathbf{y}$ (n_f×1) are the distance between two parameters in x and y directions; λ_x and λ_y are the correlation lengths (m) in x and y directions.

The reduced order algorithm requires the evaluation of unconditional parameter covariance matrix $\boldsymbol{\varepsilon}_{ff}^{(0)}$ in terms of eigenvalue $\boldsymbol{\lambda}^{(0)}$ and eigenvector $\mathbf{g}^{(0)}$. In the real-world problem, the number of parameters n_f is usually in the order of 10^3 to 10^5, and the computational cost of conducting full SVD is n_f^3 ($O(n_f^3)$). Alternately, truncated SVD with the complexity in $O(n_{ft}^2 n_f)$ can be used to approximate the original eigenvalue and eigenvector. n_{ft} is the number of randomly chose column in $\boldsymbol{\varepsilon}_{ff}^{(0)}$.

In addition to the numeric approach, the analytical solution of eigenvalues $\boldsymbol{\lambda}_n$ and eigenvectors $\mathbf{g}_n$ with brick grid and domain (Ghanem and Spanos, 2003; Zhang and Lu, 2004) is also available. In 2-D domain, they are analytically express as

$$\boldsymbol{\lambda}_n = Var\frac{2\lambda_x}{\lambda_x^2 w_{n,x}^2+1}\frac{2\lambda_y}{\lambda_y^2 w_{n,y}^2+1} \quad (21)$$

$$\mathbf{g}_n = \frac{\lambda_x w_{n,x}\cos(w_{n,x}x)+\sin(w_{n,x}x)}{\sqrt{\frac{(\lambda_x^2 w_{n,x}^2+1)L_x}{2}+\lambda_x}}\frac{\lambda_y w_{n,y}\cos(w_{n,y}y)+\sin(w_{n,y}y)}{\sqrt{\frac{(\lambda_y^2 w_{n,y}^2+1)L_y}{2}+\lambda_y}} \quad (22)$$

where $w_{n,x}$ and $w_{n,y}$ are the positive roots of the characteristic equations

$$(\lambda_x^2 w_{n,x}^2-1)\sin(w_{n,x}L_x) = 2\lambda_x w_{n,x}\cos(w_{n,x}L_x) \quad (23)$$

and

$$(\lambda_y^2 w_{n,y}^2-1)\sin(w_{n,y}L_y) = 2\lambda_y w_{n,y}\cos(w_{n,y}L_y) \quad (24)$$

where L_x and L_y are the width of model domain in *x* and *y* directions.

Notice that if the model domain is irregular (i.e., not a line, squared, or brick shape), one can first construct the eigenvalue and eigenvector for a regular domain whose size is greater than the irregular one. Afterward, the eigenvector of the irregular domain can be evaluated by

$$\mathbf{g}_{irreg} = \mathbf{C}_2\mathbf{g}_{reg} \quad (25)$$

in which $\mathbf{C}_2$ ($n_{f,irreg}\times n_{f,reg}$) is a matrix to eliminate the rows of $\mathbf{g}_{reg}$ if the corresponding grids are outside the model domain; $n_{f,reg}$ is the number of parameter of

https://doi.org/10.5194/hess-2019-622
Preprint. Discussion started: 3 January 2020
© Author(s) 2020. CC BY 4.0 License.

the regular line, squared, or brick domain; $n_{f,irreg}$ is the number of parameter of the irregular domain. $\mathbf{g}_{reg}$ and $\mathbf{g}_{irreg}$ are the eigenvectors of regular and irregular domains.

Data Error: The initial data error $\hat{\mathbf{e}}^{(0)}$ can set as zero.

Data Covariance: The unconditional covariance matrix of the observed data $\boldsymbol{\varepsilon}_{hh}^{(0)}$ is a diagonal matrix if the data error are mutually independent. Otherwise, a covariance function (e.g., eq. (20)) can be utilized to describe the unconditional correlation.

2.4. Evaluation of Covariance

The algorithm also requires the evaluation of squared root of cross-covariance $\mathbf{H}_{fh}^{(r)}$. One can evaluate the sensitivity by adjoint approach (e.g., Sykes et al., 1985; Sun and Yeh, 1990) first and substitute it into eq. (14) to derive $\mathbf{H}_{fh}^{(r)}$. The computational cost of the adjoint approach is to run the linear adjoint forward model n_w (number of observation wells) to n_d (number of states) times, depending on the model configurations (e.g., confined, unconfined, saturated, unsaturated, and the types of boundary condition, etc.).

On the other hand, a perturbation approach (e.g., forward, backward, central differences, etc.) can be utilized to directly evaluate $\mathbf{H}_{fh}^{(r)}$ so that the computation of sensitivity is eliminated. Let $G(\cdot)$ represent the groundwater flow governing equation and its Taylor expansion evaluated on $\hat{\mathbf{f}}^{(r)}+\mathbf{g}^{(r)}\delta$ is

$$G(\hat{\mathbf{f}}^{(r)}+\mathbf{g}^{(r)}\delta)=G(\hat{\mathbf{f}}^{(r)})+G'(\hat{\mathbf{f}}^{(r)})\mathbf{g}^{(r)}\delta+G''(\hat{\mathbf{f}}^{(r)})\frac{(\mathbf{g}^{(r)}\delta)^2}{2}+G'''(\hat{\mathbf{f}}^{(r)})\frac{(\mathbf{g}^{(r)}\delta)^3}{3!}+\ldots \quad (26)$$

δ is an arbitrary value controlling the accuracy of approximation. Manipulating eq.

https://doi.org/10.5194/hess-2019-622
Preprint. Discussion started: 3 January 2020
© Author(s) 2020. CC BY 4.0 License.
Hydrology and Earth System Sciences Discussions

(26) yields

$$G'(\hat{\mathbf{f}}^{(r)})\mathbf{g}^{(r)} = \mathbf{J}_{fh}^{(r)T}\mathbf{g}^{(r)} = \frac{G(\hat{\mathbf{f}}^{(r)}+\mathbf{g}^{(r)}\delta)-G(\hat{\mathbf{f}}^{(r)})}{\delta} - G''(\hat{\mathbf{f}}^{(r)})\frac{(\mathbf{g}^{(r)})^2\delta}{2} - G'''(\hat{\mathbf{f}}^{(r)})\frac{(\mathbf{g}^{(r)})^3\delta^2}{3!} - \ldots$$

(27)

Multiplying both sides with $\sqrt{\boldsymbol{\lambda}^{(r)}}$, eq. (27) becomes

$$\mathbf{H}_{fh}^{(r)} = \left[\frac{G(\hat{\mathbf{f}}^{(r)}+\mathbf{g}^{(r)}\delta)-G(\hat{\mathbf{f}}^{(r)})}{\delta} - G''(\hat{\mathbf{f}}^{(r)})\frac{(\mathbf{g}^{(r)})^2\delta}{2} - G'''(\hat{\mathbf{f}}^{(r)})\frac{(\mathbf{g}^{(r)})^3\delta^2}{3!} - \ldots\right]\sqrt{\boldsymbol{\lambda}^{(r)}} \quad (28)$$

Accordingly, $\mathbf{H}_{fh}^{(r)}$ can be approximated by

$$\mathbf{H}_{fh}^{(r)} \approx \frac{G(\hat{\mathbf{f}}^{(r)}+\mathbf{g}^{(r)}\delta)-G(\hat{\mathbf{f}}^{(r)})}{\delta}\sqrt{\boldsymbol{\lambda}^{(r)}} \quad (29)$$

and the corresponding error is

$$err = \sqrt{\boldsymbol{\lambda}^{(r)}}G''(\hat{\mathbf{f}}^{(r)})\frac{(\mathbf{g}^{(r)})^2\delta}{2} + \ldots \quad (30)$$

To evaluate $\mathbf{H}_{fh}^{(r)}$, we need to run the forward model n_{svd} (number of kept eigens) × n_{event} (number of pumping or injection events) times.

If we further evaluate $G(\cdot)$ on $\hat{\mathbf{f}}^{(r)}-\mathbf{g}^{(r)}\delta$ and combine it with $G(\hat{\mathbf{f}}^{(r)}+\mathbf{g}^{(r)}\delta)$, we have

$$G(\hat{\mathbf{f}}^{(r)}+\mathbf{g}^{(r)}\delta)-G(\hat{\mathbf{f}}^{(r)}-\mathbf{g}^{(r)}\delta) = 2\left[G'(\hat{\mathbf{f}}^{(r)})\mathbf{g}^{(r)}\delta + G'''(\hat{\mathbf{f}}^{(r)})\frac{(\mathbf{g}^{(r)}\delta)^3}{3!} + \ldots\right] \quad (31)$$

Multiplying both sides with $\sqrt{\boldsymbol{\lambda}^{(r)}}$ and $\mathbf{H}_{fh}^{(r)}$ can be approximated by

$$\mathbf{H}_{fh}^{(r)} \approx \frac{G(\hat{\mathbf{f}}^{(r)}+\mathbf{g}^{(r)}\delta)-G(\hat{\mathbf{f}}^{(r)}-\mathbf{g}^{(r)}\delta)}{2\delta}\sqrt{\boldsymbol{\lambda}^{(r)}} \quad (32)$$

The corresponding error is

$$err = \sqrt{\boldsymbol{\lambda}^{(r)}}G'''(\hat{\mathbf{f}}^{(r)})\frac{(\mathbf{g}^{(r)})^3\delta^2}{3!} + \ldots \quad (33)$$

The evaluation of more accurate $\mathbf{H}_{fh}^{(r)}$ requires the exercise of forward model $2n_{svd}$ × n_{event} times.

https://doi.org/10.5194/hess-2019-622
Preprint. Discussion started: 3 January 2020
© Author(s) 2020. CC BY 4.0 License.

2.5. Computational Advantages

The proposed reduced-order dual state-parameter inverse algorithm is efficient when the number of kept leading eigens (n_{svd}) is less than 1500. If the ratio of domain size and correlation length is huge, large n_{svd} value increase the computational cost of SVD ($O(n_{kl}^3)$). Furthermore, evaluating $\mathbf{H}_{fh}^{(r)}$ through the forward or backward finite difference approach is efficient for many types of forward models (e.g., variable saturated diffusion equation, advection diffusion equation). It only requires executing the forward model for n_{svd}×n_{event} (number of pumping events) times. On the contrary, when the forward model is elegant (e.g., fully saturated diffusion equation), it is cost-effective to evaluate the sensitivity of state with respect to unknown parameter (eq. 14, $\mathbf{J}_{fh}^{(r)}$) through the adjoint method. Only n_w (number of observation wells) forward runs is required. In addition, updating state variable errors is efficient when n_d (number of state variable) is less than 10000. The most expensive additional computational cost is to solve the inverse n_d×n_d matrix (eqs. 12 and 13) through either Cholesky or QR decompositions (matrix multiplication is an easy task under the parallel computing scheme).

3. Algorithm Verification

In this section, three cases are used to examine the robustness of the proposed algorithm. The first and second cases involve hydraulic tomographic surveys in a synthetic aquifer without and with observation error, respectively. The third case is a 2-D application of tomography experiment in the field site.

The coefficient of determination (R^2) and the mean squared error (i.e., L_2 norm), defined as

https://doi.org/10.5194/hess-2019-622
Preprint. Discussion started: 3 January 2020
© Author(s) 2020. CC BY 4.0 License.

$$R^2 = \left[\frac{(\mathbf{f}^* - \overline{\mathbf{f}}^*)^T (\hat{\mathbf{f}}^{(r)} - \overline{\hat{\mathbf{f}}}^{(r)})}{n_f std(\mathbf{f}^*) std(\hat{\mathbf{f}}^{(r)})} \right]^2 \quad (34)$$

and

$$L_2 = \frac{(\mathbf{f}^* - \hat{\mathbf{f}}^{(0)})^T (\mathbf{f}^* - \hat{\mathbf{f}}^{(0)})}{n_f} \quad (35)$$

are utilized to evaluate the similarity between the reference and estimated parameter fields. Overbar represents the average. $std(\cdot)$ stands for the standard deviation.

3.1. Observation-Error Free Synthetic Case

The observation-error free synthetic case considers transient state HT in a two-dimensional horizontal confined aquifer of 30×30 square elements (figure 1). Each element is 1 (m)×1 (m). The aquifer is bounded by the constant head boundary (30 m). The initial head is uniform (30 m) everywhere.

(a) Forward Model

The reference field (figure 1) is generated using a spectral method (Gutjahr, 1989; Robin et al., 1993) with mean geometric T of one (m^2/day), variance of ln$T$ of one (-), and correlation scales of 10 (m) at both x and y directions. Eight wells (white dots) are evenly installed in the aquifer to collect the aquifer responses induced by three sequential pumping tests from early time till the system reaches steady state. The pumping wells are labeled with squares. The noise free observed heads only contain the numerical error (e.g., round-off and truncation errors), and its value is smaller than 10^{-7} (m). The S is a constant value of 0.001 (-). The initial time step is 0.001 (day) and the maximum time step is 1 (day).

(b) Inverse Model

Assume S is known and we would like to estimate the spatial T distribution. The

https://doi.org/10.5194/hess-2019-622
Preprint. Discussion started: 3 January 2020
© Author(s) 2020. CC BY 4.0 License.

initial mean T ($\hat{\mathbf{f}}^{(0)}$) is one (m^2/day), variance of ln$T$ ($\boldsymbol{\varepsilon}_{ff}^{(0)}$) is one (-), variance of observed head ($\boldsymbol{\varepsilon}_{hh}^{(0)}$) is 10^{-4} (m^2), and the correlation lengths λ_x and λ_y are 10 (m).

(c) **Results of Estimate**

Figure 2 shows the performances of the estimated T value using old algorithm (SLE) and figure 3 presents the performances using the new algorithm. Figure 2a presents the evolutions of mean squared error between the observed and simulated heads (L_2 norm) and the spatial variance of ln$T$ (Var ln$T$) during the calibration process. Figure 2b is the calibrated head at the final iteration. Figures 2c and 2d are the final and best estimated T field, respectively. Figure 2e and f are the scatter plots of the estimated T verses reference T corresponding to the final (figure 2c) and best (figure 2d) estimated T fields. As displayed in figure 2a, after L_2 norm approaches steady, the spatial variance of estimated T (pink line) still increases with a constant rate. The gaining of spatial variation of estimated T values comes from the over calibrated observed head. Due to the natural of least squared algorithm (e.g., minimizing the mean squared error of state variables), the algorithm compensates the numeric errors by adjusting the estimated T to unreasonably high and low values, although the general spatial trend of the estimated T fields remains similar. As the result, compare to the best estimate of T field (figure 2d and f), the final estimate diverges (figure 2c and e).

On the contrary, estimate using the new algorithm does not encounter the divergence issue. As shown in the calibration process (figure 3a), the spatial variance of estimated T (pink line) reaches steady after L_2 decays to the value of 10^{-10} (i.e., magnitude of numeric error). The final estimated field (figure 3c) converges and the performances in terms of the statistical indices (figure 3d), namely L_2, R^2 (determination coefficient), or the slope and intercept of the fitted linear relationship between the estimates and the true values, are equally good as the best estimate by the previous algorithm (figure 2c). In other word, the new algorithm eliminates the over fitting issue.

3.2. Noisy Synthetic Case

This example aims to reveal the advantages of the algorithm when the measurement errors are presented. To accomplish this goal, the Gaussian noises with standard deviation of 10^{-3} (m) are superimposed on the observed heads discussed in section 3.1. The design of inverse model is identical with those explained in section 3.1.

Figure 4 shows the performances (evolution of calibration process, head fitting, contour of the estimate field, and the scatter plot between the estimate and reference fields) of the estimated T value using original algorithm, and figure 5 presents the performances using the new one. By comparing the final estimate with the manually selected best estimate of original SLE (figure 4d and f), the final estimated T field diverges as indicated by the increase in variance of ln$T$ (pink line in figure 4a), unreasonable high and low values (red and blue spots in figure 4c) of the final estimated T fields, and the uncorrelated estimate and reference ln$T$ values (figure 4e). On the contrary, the final estimate using the proposed algorithm shows that the estimated field converges to the reasonable spatial pattern and values. The variance of ln$T$ (pink line in figure 5a) approaches stable and the simulated heads reproduce the adjusted observed heads (sum of observed heads and estimated head errors, figure 5b). Furthermore, the contour map and scatterplot of the final estimate (figure 5c and d) suggest the estimated field is close to the manually selected best estimate of original SLE (figure 4d and f) and the reference (figure 1). This means the new method no longer overestimate the parameter fields and can automatically converge to an optimal estimate under the given constrains.

3.3. Field Data

The proposed algorithm is applied to a river stage tomographic survey conducted in Pingtun Plain, Taiwan. It is a 1200 km^2 catchment with three major rivers penetrating from the north to south (figure 6). The plain is bound by foothills and river valleys at the north, faults at the west and east, and the shoreline at the south. As illustrated in figure 6b, the geology inferred from well logs shows that the upstream subsurface is consist of gravel. Follows by the layered sand and clay structure at middle and down streams. The regions with unconsolidated coarse sediments (gravel and sand) are aquifer and with fine sediments (silt and clay) are aquitard. The aquitard is characterized as marine deposition because abundant fossils such as shells and foraminifera live in the shallow marine and lagoon are discovered. The aquifer is characterized as non-marine deposition. Figure 6c presents the stream stage and groundwater level variations during 2006. The average annual rainfall is 2500 mm, with most of the precipitation happen between May and September.

We focus on characterizing the heterogeneity of shallow aquifer because it is the major water source of agriculture, industrial, and municipal water supply. The average aquifer thickness is 40 m. This catchment is discretized into a two-dimensional horizontal confined aquifer with 5619 elements. Each element is 0.5 (km)×0.5 (km). There are 36 monitoring wells evenly placed across the catchment and measuring the hourly groundwater level variation of the aquifer since 1998. The aquifer is bounded by the time varying head boundary. The time varying heads along the boundary are extrapolated by kriging using the observed head collected from all of the monitoring wells. Water levels collected from stream gauges are incorporated into the diffusion wave equation to estimate the stream stages along the river. These estimated stages

https://doi.org/10.5194/hess-2019-622
Preprint. Discussion started: 3 January 2020
© Author(s) 2020. CC BY 4.0 License.

are then treated as the prescribed head in the groundwater model. The initial groundwater level is estimated by spinning up the model for 6 years prior to June 2006 utilizing the effective *T* (1 (m^2/day)), effective *S* (10^{-5} (-)), time varying head boundary, and stream stage variations.

The denoised groundwater levels from June to September 2006 are selected using the strategy (i.e., wavelet) discussed in Wang et al. (2017). There is a total of 1440 measured heads selected for river stage tomographic survey. The initial mean *T* ($\hat{\mathbf{f}}^{(0)}$) is 1 (m^2/day), variance of ln*T* ($\boldsymbol{\varepsilon}_{ff}^{(0)}$) is one (-), variance of observed head ($\boldsymbol{\varepsilon}_{hh}^{(0)}$) is 10^{-4} (m^2), and the correlation lengths λ_x and λ_y are 15 (km). For simplicity, we assume *S* is uniform and focus on estimating the spatial *T* distribution. The patterns of estimated *T* fields should be consistent with the hydraulic diffusivity field.

Figure 7 presents the calibration using the original SLE algorithm. The increasing of variance of ln*T* (figure 7a) near the end of iteration (iteration 100) suggests the estimate diverges, although the parameter field reproduces the observed drawdowns (figure 7b). The unreasonable huge spatial *T* variation corresponds to the significantly low and high values on the contour map of the final estimate field (figure 7c). The contour map of manually selected best estimate is shown in figure 7d and the calibrated heads are similar with those in figure 7b.

Figure 8 shows the estimate using the new algorithm. The performance clearly demonstrates the robustness and usefulness of the new algorithm on characterizing the subsurface heterogeneity. Compared with the variance of ln*T* in figure 7a, it stabilizes at the end of iteration (figure 8a) while still reproduces the adjusted observed heads (figure 8b). The estimated field (figure 8c) shares the similar spatial patterns with the manually selected one (figure 7d).

To further examine the reliability of the estimate, the estimated *T* field is

https://doi.org/10.5194/hess-2019-622
Preprint. Discussion started: 3 January 2020
© Author(s) 2020. CC BY 4.0 License.

compared with the map of geological sensitivity regions (figure 9) delineated by the Department of Central Geology Survey, Taiwan. The geological sensitivity regions represent the major areas water recharges the aquifer. They are categorized by core samples, geophysics (e.g., electric resistivity), and geochemical survey. In general, the deposition of geological sensitivity region is gravel and the aquifer thickness is greater than 100 m (blue areas in figure 6b). Compared figure 9 with figure 7d and 8c, the high *T* regions located near the upper streams (red areas) are in parallel with the geological sensitivity regions.

4. Conclusion

In this paper, a reduced order geostatistical model is developed to account for the subsurface heterogeneity. This method includes the evaluation of the errors of state variables and unknown parameters to improve the robustness of convergence. The over fitting problem (i.e., diverged estimated parameter fields) is leveraged by considering these errors into the calibration process. The memory burden (i.e. high dimensional parameter covariance) and requirement of domain shape (e.g., brick or rectangle) are also relieved by approximating the parameter covariance matrix through limited number of leading eigenvalues and eigenvectors using SVD. Meanwhile, the computation of sensitivity is replaced by the direct evaluation of cross-covariance through the finite differencing method. The modification relaxes barrier of implementing this inverse algorithm to different disciplines because the derivation of adjoint state method is no longer necessary. Lastly, as the stability of convergence is robust and the evaluation of cross-covariance (sensitivity) is efficient, the proposed algorithm is valuable and attractive for multi-discipline scientific problems, especially useful and convenient for assimilating different types of measurements.

© Author(s) 2020. CC BY 4.0 License.

5. Acknowledgment

This research is in part by U.S. Civilian Research and Development Foundation (CRDF Global) under the award number (DAA2-15-61224-1): Hydraulic tomography in shallow alluvial sediments: Nile River Valley, Egypt. The authors gratefully acknowledge the financial support by Minster of Science and Technology, Taiwan under award number 108-2116-M-002-029-MY3.

6. Reference

Ait-El-Fquih, B., El Gharamti, M., and Hoteit, I.: A Bayesian consistent dual ensemble Kalman filter for state-parameter estimation in subsurface hydrology, Hydrol. Earth Syst. Sci., 20, 3289-3307, https://doi.org/10.5194/hess-20-3289-2016, 2016.

Cirpka, O. A., and P. K. Kitanidis: Sensitivity of temporal moments calculated by the adjoint-state method and joint inversing of head and tracer data, Adv. Water Resour., 24(1), 89–103, doi:10.1016/S0309-1708(00)00007-5, 2000.

Field G, Tavrisov G, Brown C, Harris A, Kreidl OP: Particle filters to estimate properties of confined aquifers. Water Resour. Manag., 30(9):3175–3189, https://doi.org/10.1007/s11269-016-1339-1, 2016.

Ghanem, R. G., & Spanos, P. D.: Stochastic finite elements: A spectral approach. North Chelmsford, MA: Courier Corporation, 2003.

Ghorbanidehno, H., Kokkinaki, A., Li, J.Y., Darve, E., Kitanidis, P.K.: Real-time data

© Author(s) 2020. CC BY 4.0 License.

assimilation for large-scale systems: the spectral Kalman filter. Adv. Water Resour., 86, 260-272, doi:10.1016/j.advwatres.2015.07.017, 2015.

Gutjahr, A. L.: Fast Fourier transforms for random field generation, project report for Los Alamos grant, Contract 4-R58-2690R, Dep. of Math., N. M. Tech., Socorro, 1989.

Horning, S., J. Sreekanth, A. Bardossy: Computational efficient inverse groundwater modeling using Random Mixing and Whittaker–Shannon interpolation, Adv. Water Resour., 123, 109-119, doi:10.1016/j.advwatres.2018.11.012, 2019.

Illman, W. A., S. J. Berg, and Z. Zhao: Should hydraulic tomography data be interpreted using geostatistical inverse modeling? A laboratory sandbox investigation, Water Resour. Res., 51, 3219–3237, doi:10.1002/2014WR016552, 2015.

Kitanidis, P. K.: Quasi-linear geostatistical theory for inversing, Water Resour. Res., 31(10), 2411– 2419, doi:10.1029/95WR01945, 1995.

Kitanidis, P. K., and Lee, J.: Principal Component Geostatistical Approach for large-dimensional inverse problems, Water Resour. Res., 50, 5428-5443, doi:10.1002/2013WR014630, 2014.

Kitanidis PK. Compressed state Kalman filter for large systems, Adv. Water Resour., 76, 120–126, 2015, doi:10.1016/j.advwatres.2014.12.010.

Leng, C. H., and Yeh, H. D.: Aquifer parameter identification using the extended

© Author(s) 2020. CC BY 4.0 License.

Kalman filter, Water Resour. Res., 39, 1062, doi:10.1029/2001WR000840, 3, 2003.

Li, J. Y., Ambikasaran, S., Darve, E. F., and Kitanidis, P. K.: A Kalman filter powered by H^2-matrices for quasi-continuous data assimilation problems, Water Resour. Res., 50, 3734-3749, doi:10.1002/2013WR014607, 2014.

Li, J. Y., Kokkinaki, A., Ghorbanidehno, H., Darve, E. F., and Kitanidis, P. K.: The compressed state Kalman filter for nonlinear state estimation: Application to large-scale reservoir monitoring, Water Resour. Res., 51, 9942– 9963, doi:10.1002/2015WR017203, 2015.

Lin, Y., O'Malley, D., and Vesselinov, V. V.: A computationally efficient parallel Levenberg - Marquardt algorithm for highly parameterized inverse model analyses, Water Resour. Res., 52, 6948– 6977, doi:10.1002/2016WR019028, 2016.

Lin, Y., Le, E. B., O'Malley, D., Vesselinov, V. V., and Bui-Thanh, T.: Large-scale inverse model analyses employing fast randomized data reduction, Water Resour. Res., 53, 6784– 6801, doi:10.1002/2016WR020299, 2017.

Liu, X., Zhou, Q., Birkholzer, J., and Illman, W. A.: Geostatistical reduced-order models in underdetermined inverse problems, Water Resour. Res., 49, 6587– 6600, doi:10.1002/wrcr.20489, 2013.

Liu, X., Zhou, Q., Kitanidis, P. K., and Birkholzer, J. T.: Fast iterative implementation of large-scale nonlinear geostatistical inverse modeling, Water Resour. Res., 50, 198–207, doi:10.1002/2012WR013241, 2014.

© Author(s) 2020. CC BY 4.0 License.

Nowak, W., and O. A. Cirpka: Geostatistical inference of hydraulic conductivity and dispersivities from hydraulic heads and tracer data, Water Resour. Res., 42, W08416, doi:10.1029/2005WR004832, 2006.

Nowak, W., Litvinenko, A.: Kriging and spatial design accelerated by orders of magnitude: combining low-rank covariance approximations with fft-techniques. Math. Geosci. 45 (4), 411-435, doi:10.1007/s11004-013-9453-6, 2013.

Pagh, R.: Compressed matrix multiplication. ACM Trans. Comput. Theory, 5(3):9:1–9:17, doi: 10.1145/2493252.2493254, 2013.

Robin, M. J. L., A. L. Gutjahr, E. A. Sudicky, and J. L. Wilson: Cross-correlated random field generation with the direct Fourier transform method, Water Resour. Res., 29, 2385-2397, doi:10.1029/93WR00386, 1993.

Saibaba, A. K., and Kitanidis, P. K.: Efficient methods for large-scale linear inversion using a geostatistical approach, Water Resour. Res., 48, W05522, doi:10.1029/2011WR011778, 2012.

Schöniger, A., Nowak, W., and Hendricks Franssen, H.-J.: Parameter estimation by ensemble Kalman filters with transformed data: Approach and application to hydraulic tomography, Water Resour. Res., 48, W04502, doi:10.1029/2011WR010462, 2012.

Sun, N.-Z., and W. W.-G. Yeh: Coupled inverse problems in groundwater modeling: 1.

© Author(s) 2020. CC BY 4.0 License.

Sensitivity analysis and parameter identification, Water Resour. Res., 26(10), 2507-2525, doi:10.1029/WR026i010p02507, 1990.

Sykes, J. F., J. L. Wilson, and R. W. Andrews: Sensitivity Analysis for Steady-State Groundwater Flow Using Adjoint Operators, Water Resour. Res., 21(3), 359-371, doi:10.1029/WR021i003p00359, 1985.

Tsai, J.-P., Yeh, T.-C. J., Cheng, C.-C., Zha, Y., Chang, L.-C., Hwang, C., Wang, Y.-L., Hao, Y.: Fusion of time-lapse gravity survey and hydraulic tomography for estimating spatially varying hydraulic conductivity and specific yield fields. Water Resour. Res., 53, 8554-8571. doi:10.1002/2017WR020459, 2017.

Vesselinov, V., S. Neuman, and W. Illman: Three-dimensional numerical inversion of pneumatic cross-hole tests in unsaturated fractured tuff 1. Methodology and borehole effects, Water Resour. Res., 37, 3001–3017, doi:10.1029/2000WR000133, 2001.

Yeh, T.-C. J., M. Jin, and S. Hanna: An Iterative Stochastic Inverse Method: Conditional Effective Transmissivity and Hydraulic Head Fields, Water Resour. Res., 32(1), 85-92, doi:10.1029/95WR02869, 1996.

Yeh, H. D., and Y. C. Huang: Parameter estimation for leaky aquifers using the extended Kalman filter, and considering model and data measurement uncertainties, J. Hydrol., 302 (1–4), 28-45, doi:10.1016/j.jhydrol.2004.06.035, 2005.

Yin, D., and W. A. Illman: Hydraulic tomography using temporal moments of drawdown recovery data: A laboratory sandbox study, Water Resour. Res., 45,

© Author(s) 2020. CC BY 4.0 License.

W01502, doi:10.1029/2007WR006623, 2009.

Zha, Y., T.-C. J. Yeh, W. A. Illman, W. Zeng, Y. Zhang, F. Sun, L. Shi: A reduced-order successive linear estimator for geostatistical inversion and its application in hydraulic tomography. Water Resour. Res., 54, 1616-1632, doi:10.1002/2017WR021884, 2018.

Zhang, D. and Lu, Z.: An efficient, high-order perturbation approach for flow in random porous media via Karhunen-Loève and polynomial expansions. Journal of Computational Physics, 194 (2), 773– 794. https://doi.org/10.1016/j.jcp.2003.09.015, 2004.

Zhang, H., Hendricks Franssen, H.-J., Han, X., Vrugt, J. A., and Vereecken, H.: State and parameter estimation of two land surface models using the ensemble Kalman filter and the particle filter, Hydrol. Earth Syst. Sci., 21, 4927-4958, https://doi.org/10.5194/hess-21-4927-2017, 2017.

Zhang, J., Lin, G., Li, W., Wu, L., Zeng, L.: An iterative local updating ensemble smoother for estimation and uncertainty assessment of hydrologic model parameters with multimodal distributions. Water Resour. Res., 54, 1716-1733, doi:10.1002/2017WR020906, 2018.

Zunino A. and Mosegaard K.: An efficient method to solve large linearizable inverse problems under Gaussian and separability assumptions. Computers and Geosciences, 122, 77-86, doi:10.1016/j.cageo.2018.09.005, 2019.

https://doi.org/10.5194/hess-2019-622
Preprint. Discussion started: 3 January 2020
© Author(s) 2020. CC BY 4.0 License.

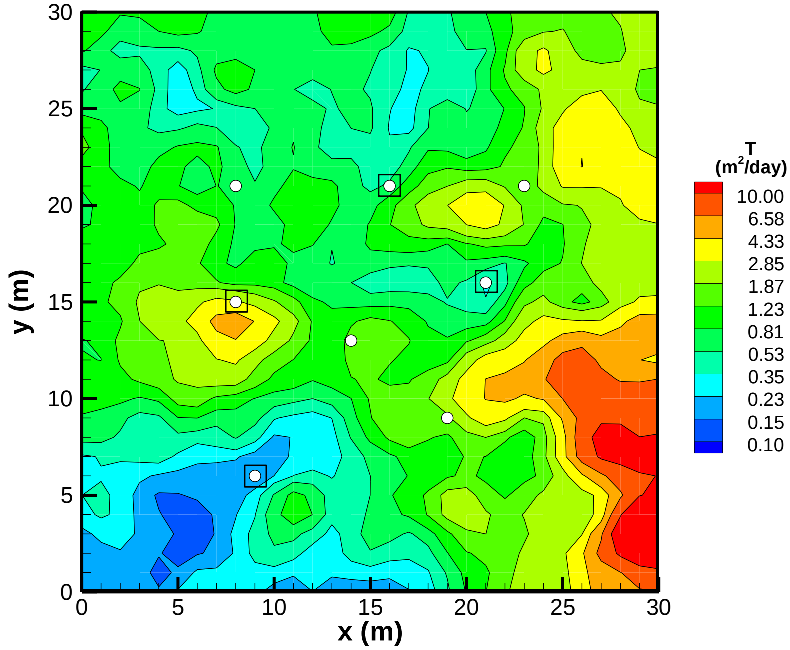

669
670 Figure 1. Reference hydraulic transimissivity T (m^2/day) field. The white dots
671 represent monitoring wells and the squared are pumping wells. Four boundaries are
672 the constant head.
673

© Author(s) 2020. CC BY 4.0 License.
Hydrology and Earth System Sciences
Discussions
Open Access
EGU

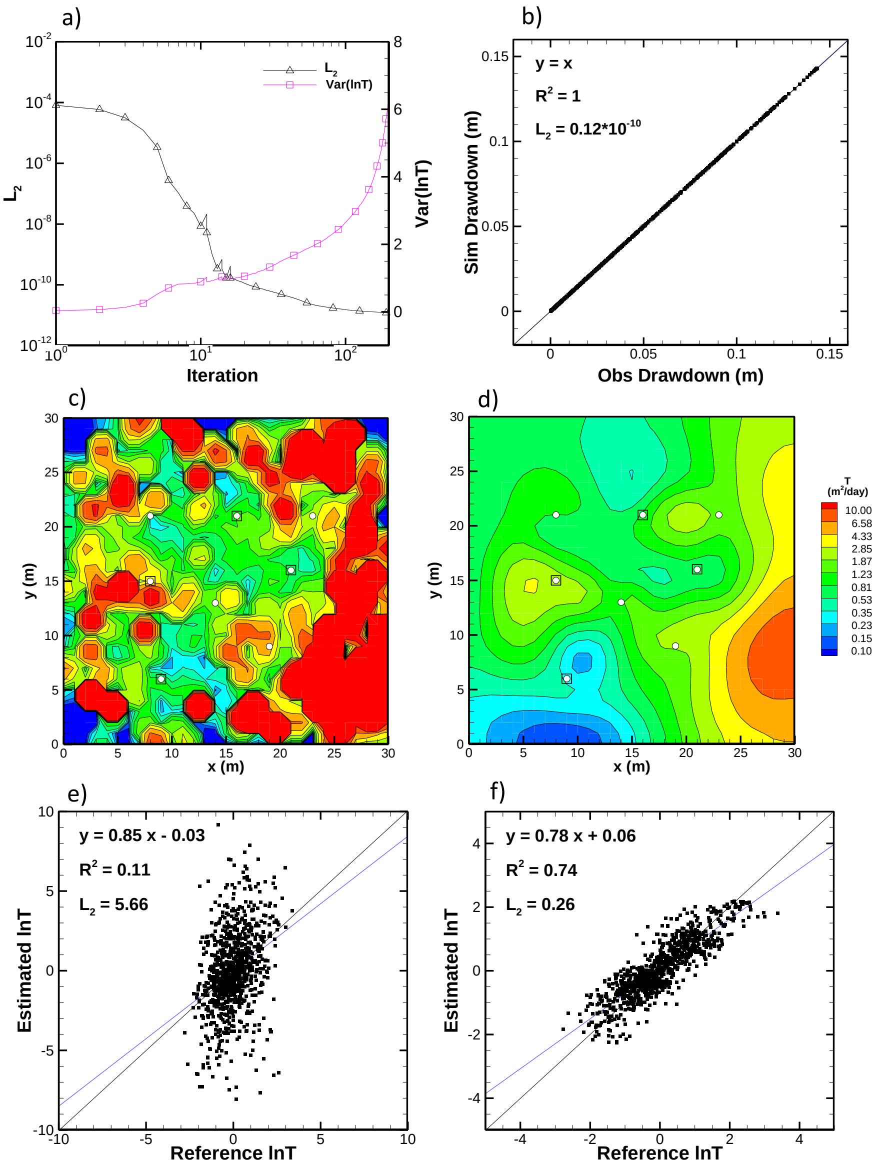

Figure 2. The estimated hydraulic transmissivity T (m^2/day) field using noise free observed head and old algorithm. a) The evolutions of mean squared error between the observed and simulated heads (L_2 norm) and the spatial variance of ln$T$ (Var ln$T$) during the calibration process. b) The calibrated head of the final iteration. c) The final estimated T field. d) The best estimated T field. e) The scatter plots of final estimated verses reference ln$T$. f) The scatter plots of best estimated verses reference ln$T$.

https://doi.org/10.5194/hess-2019-622
Preprint. Discussion started: 3 January 2020
© Author(s) 2020. CC BY 4.0 License.

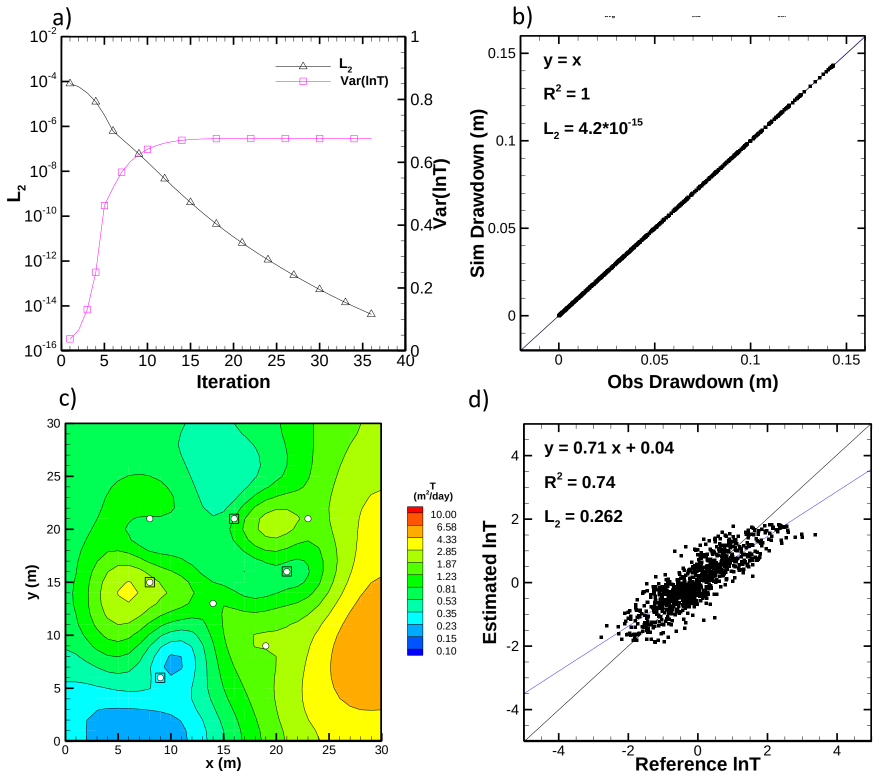

Figure 3. The estimated hydraulic transmissivity T (m^2/day) field using noise free observed head and new algorithm. a) The evolutions of mean squared error between the observed and simulated heads (L_2 norm) and the spatial variance of ln$T$ (Var ln$T$) during the calibration process. b) The calibrated head of the final iteration. c) The final estimated T field. d) The scatter plots of final estimated verses reference ln$T$.

https://doi.org/10.5194/hess-2019-622
Preprint. Discussion started: 3 January 2020
© Author(s) 2020. CC BY 4.0 License.

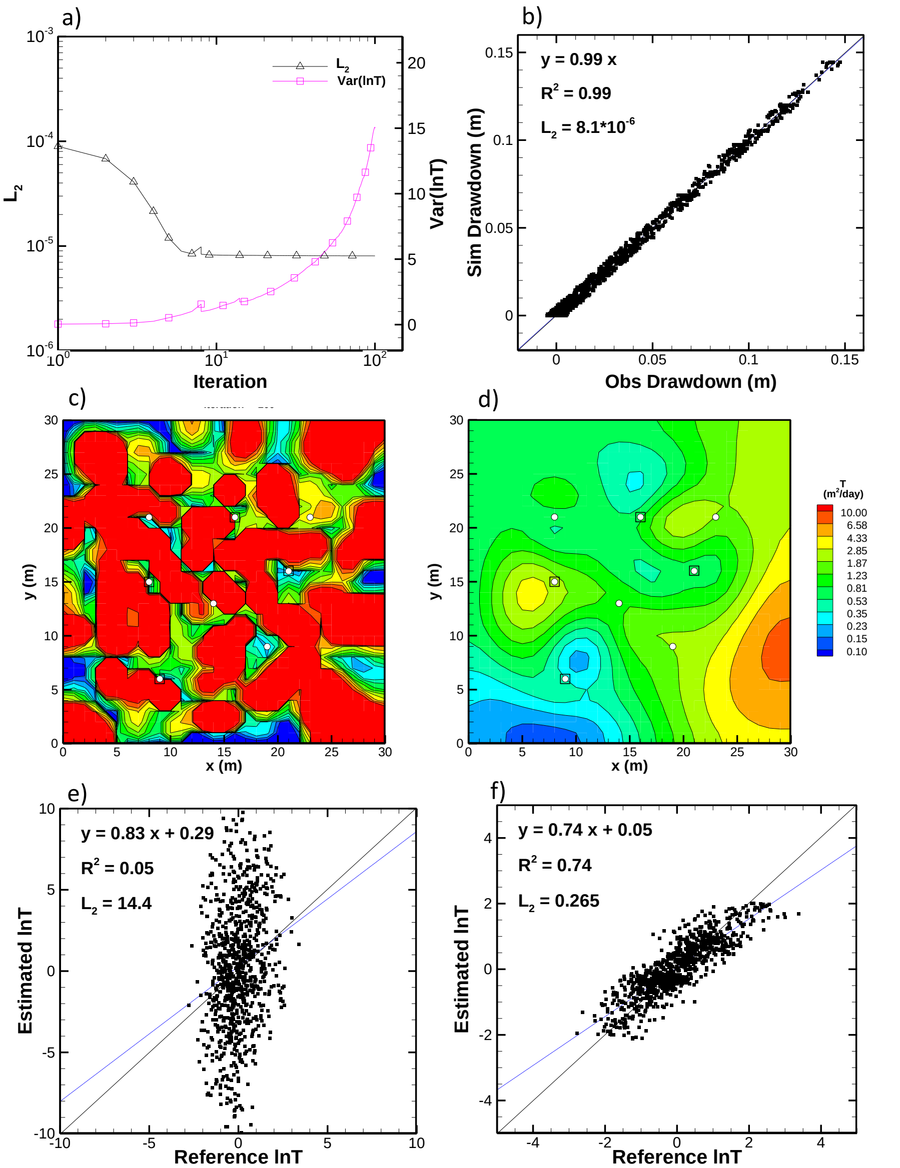

Figure 4. The estimated hydraulic transmissivity T (m^2/day) field using noisy observed head and old algorithm. a) The evolutions of mean squared error between the observed and simulated heads (L_2 norm) and the spatial variance of ln$T$ (Var ln$T$) during the calibration process. b) The calibrated head of the final iteration. c) The final estimated T field. d) The best estimated T field. e) The scatter plots of final estimated verses reference ln$T$. f) The scatter plots of best estimated verses reference ln$T$.

https://doi.org/10.5194/hess-2019-622
Preprint. Discussion started: 3 January 2020
© Author(s) 2020. CC BY 4.0 License.
Hydrology and Earth System Sciences
Discussions

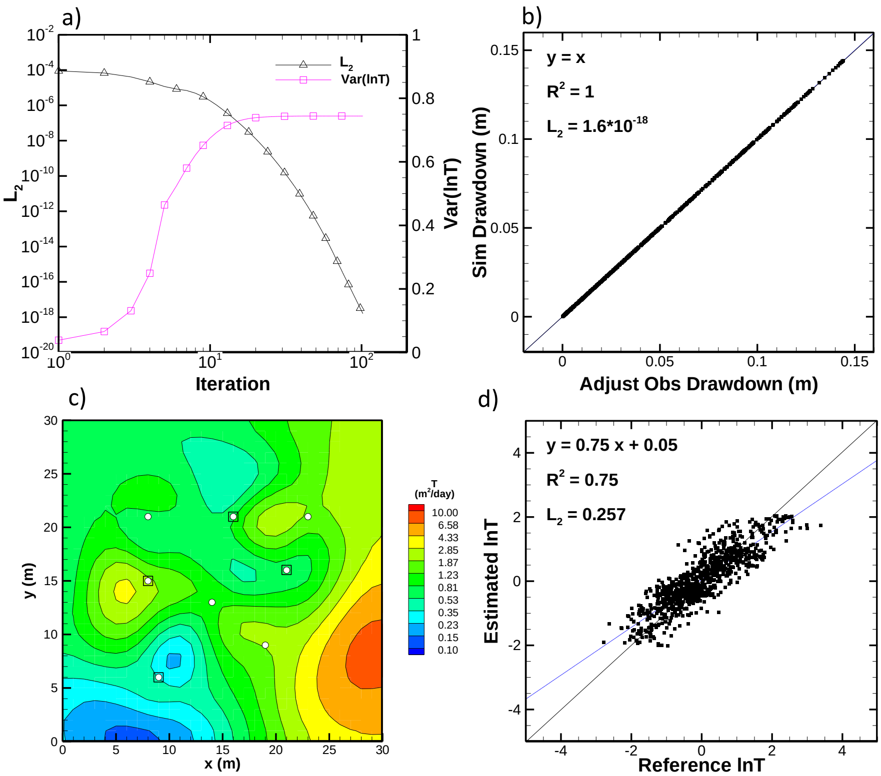

Figure 5. The estimated hydraulic transmissivity T (m^2/day) field using noisy observed head and new algorithm. a) The evolutions of mean squared error between the observed and simulated heads (L_2 norm) and the spatial variance of ln$T$ (Var ln$T$) during the calibration process. b) The calibrated heads verse adjusted observed heads (observed head + estimated error) of the final iteration. c) The final estimated T field. d) The scatter plots of final estimated verses reference ln$T$.

https://doi.org/10.5194/hess-2019-622
Preprint. Discussion started: 3 January 2020
© Author(s) 2020. CC BY 4.0 License.

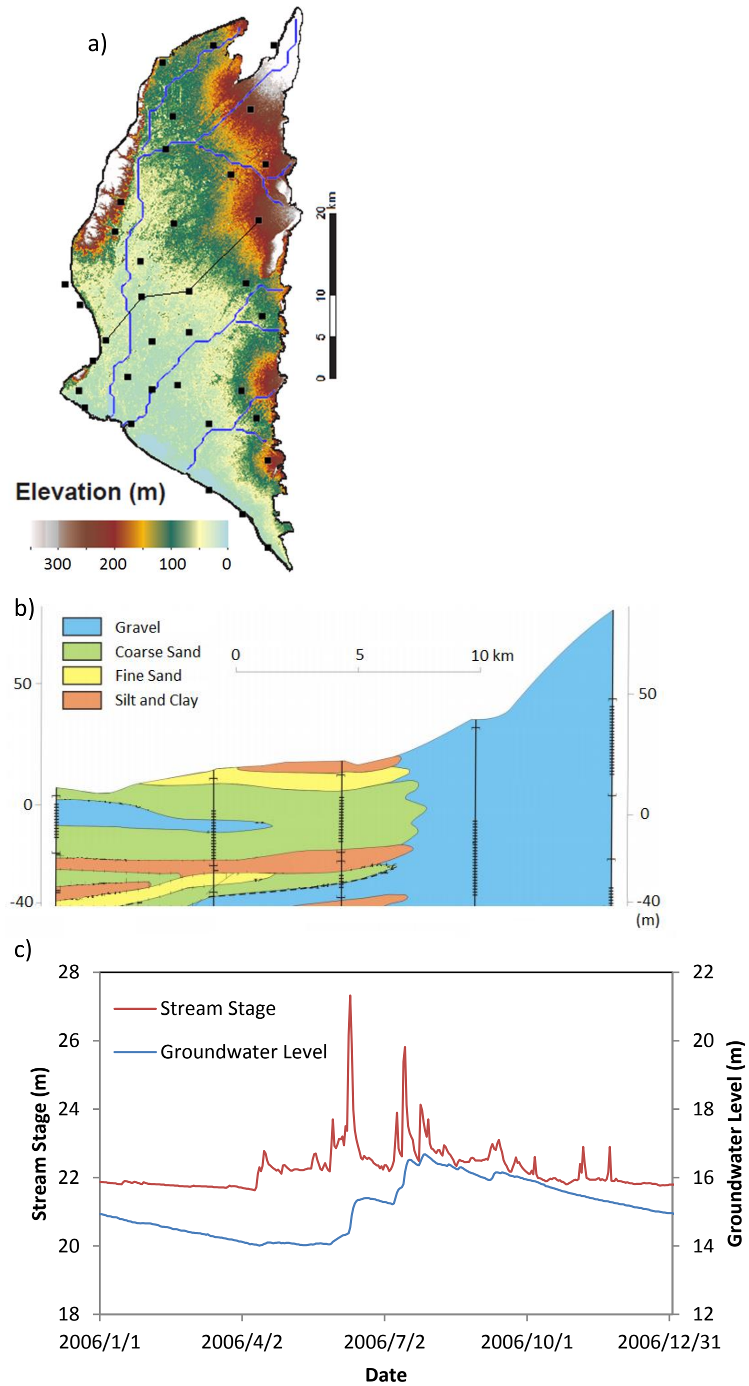

https://doi.org/10.5194/hess-2019-622
Preprint. Discussion started: 3 January 2020
© Author(s) 2020. CC BY 4.0 License.

Figure 6. a) Topography of the study plain. The blue lines represent rivers and the black rectangles are groundwater monitoring wells. The black line is geological cross section. b) Geological cross section. c) Stream stage and groundwater level variations during 2006. a) and b) are modified from the website of Water Resources Agency, the administrative agency of the Ministry of Economic Affairs in Taiwan.

https://doi.org/10.5194/hess-2019-622
Preprint. Discussion started: 3 January 2020
© Author(s) 2020. CC BY 4.0 License.

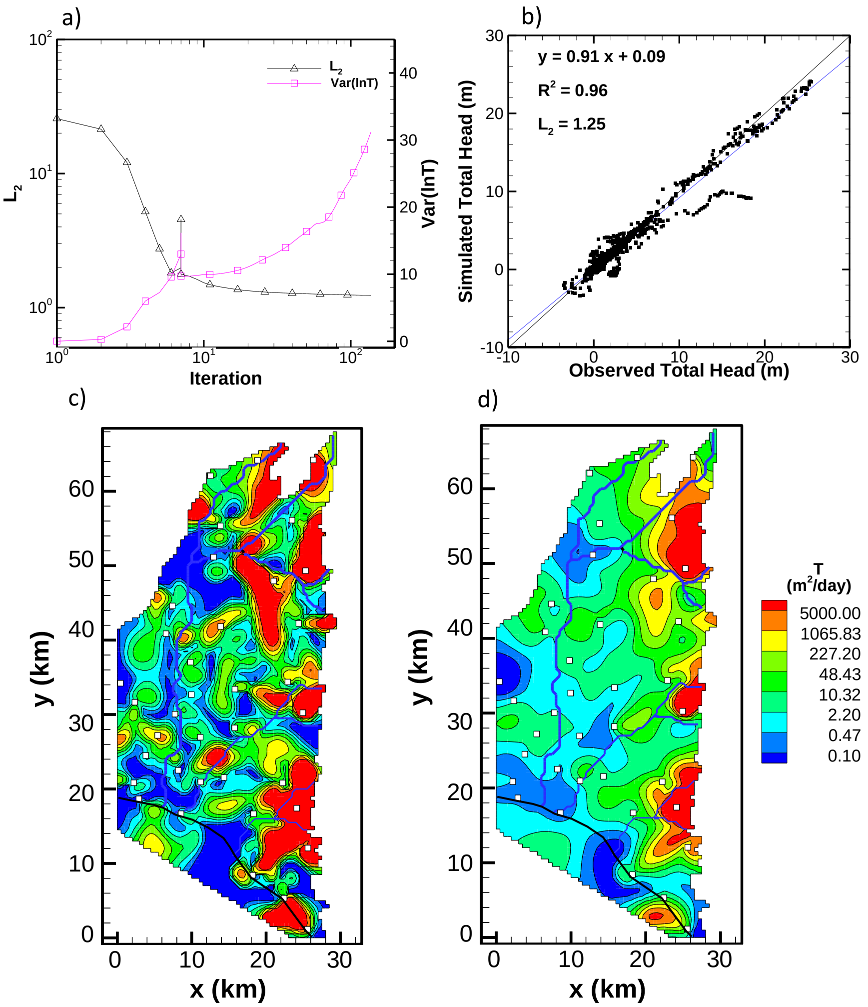

Figure 7. The estimated hydraulic transmissivity T (m^2/day) field using observed head in the field and old algorithm. a) The evolutions of mean squared error between the observed and simulated heads (L_2 norm) and the spatial variance of ln$T$ (Var ln$T$) during the calibration process. b) The calibrated head of the final iteration. c) The final estimated T field. d) The best estimated T field. The white squares represent wells, the blue lines are rivers, and the black line is shoreline.

© Author(s) 2020. CC BY 4.0 License.

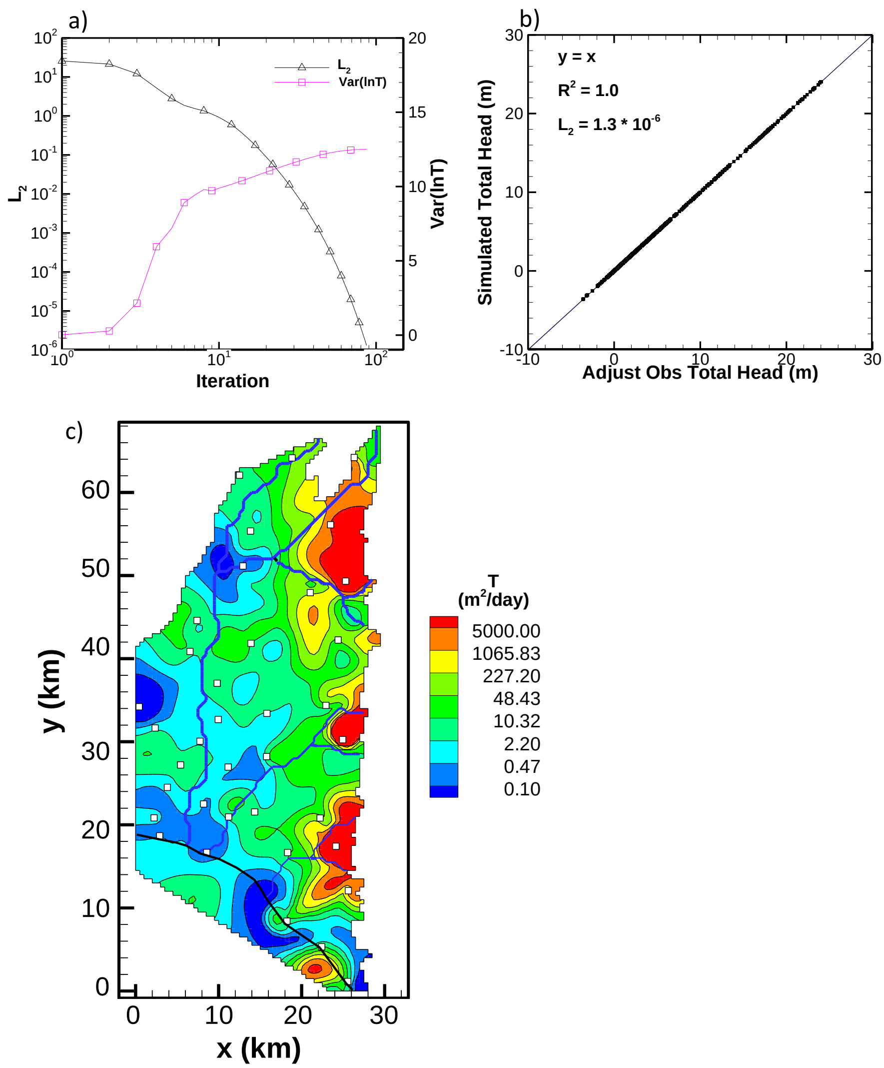

Figure 8. The estimated hydraulic transmissivity T (m^2/day) field using observed head in the field and new algorithm. a) The evolutions of mean squared error between the observed and simulated heads (L_2 norm) and the spatial variance of ln$T$ (Var ln$T$) during the calibration process. b) The calibrated heads verse adjusted observed heads (observed head + estimated error) of the final iteration. c) The final estimated T field. The white squares represent wells, the blue lines are rivers, and the black line is shoreline.

https://doi.org/10.5194/hess-2019-622
Preprint. Discussion started: 3 January 2020
© Author(s) 2020. CC BY 4.0 License.

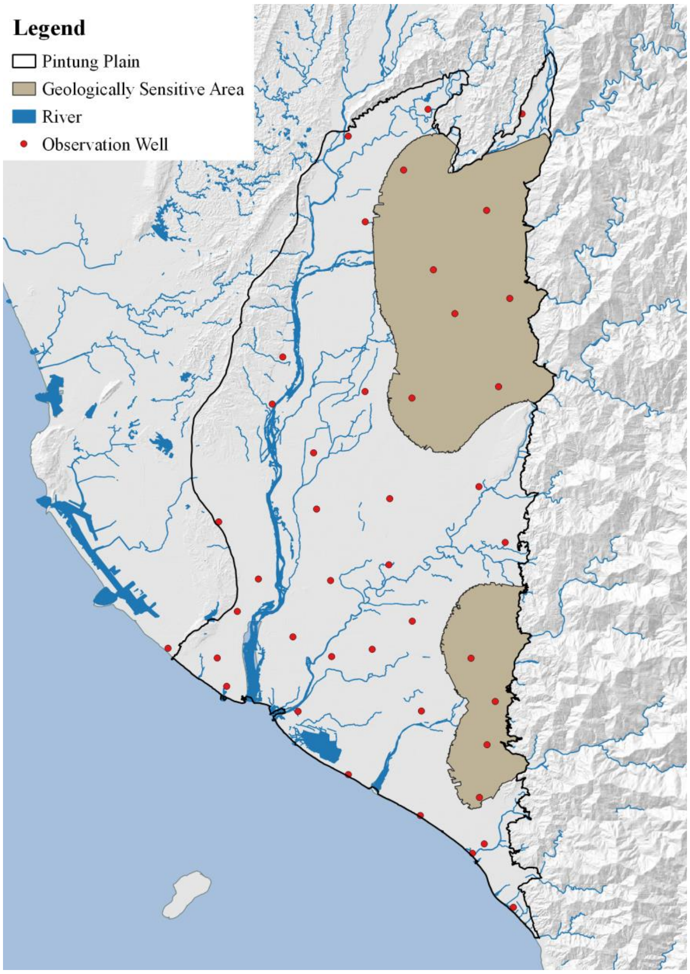

Figure 9. Geological sensitivity regions delineated by the Department of Central Geology Survey, Taiwan.

https://doi.org/10.5194/hess-2019-622
Preprint. Discussion started: 3 January 2020
© Author(s) 2020. CC BY 4.0 License.

Code/Data availability

The code and data are available upon the request through corresponding author.

Author contribution

Y.-L. Wang designed the study, carried out the analysis, interpreted the data, and wrote the paper. T.-C. Jim Yeh and J.-P. Tsai provided the financial support and helped finalize the paper.

Competing interests

The authors declare that they have no conflict of interest.